Journal of Colloid and Interface Science 665 (2024) 263–273

Contents lists available at ScienceDirect

Journal of Colloid And Interface Science

journal homepage: www.elsevier.com/locate/jcis

Regular Article

Interplay of electrokinetic effects in nonpolar solvents for electronic paper displays

Mohammad Khorsand Ahmadi [a,b], Wei Liu [a,b,c], Jan Groenewold [c,d], Jaap M.J. den Toonder [a,b], Alex Henzen [c], Hans M. Wyss [a,b,*]

[a] Department of Mechanical Engineering, Microsystems, Eindhoven University of Technology, Eindhoven, 5600 MB, Netherlands
[b] Institute for Complex Molecular Systems [ICMS], Eindhoven University of Technology, Eindhoven, 5600 MB, Netherlands
[c] South China Academy of Advanced Optoelectronics, Electronic Paper Display Institute, Guangzhou 510006, China
[d] Department of Physical and Colloid Chemistry, Debye Institute for Nanomaterials Science, Utrecht University, Padualaan 8, Utrecht, 3584 CH, Netherlands

GRAPHICAL ABSTRACT

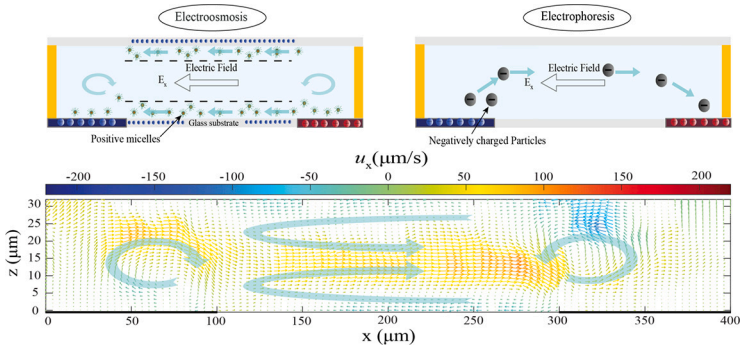

Interplay of electrokinetic effects: Driven by the applied electric field, both *electro-osmosis* (EO, top left), which drives a flow along the surfaces of the fluidic cell, and *electrophoresis* (EP, top right), which drives a migration of particles relative to the background liquid, occur in our system. A typical example of the resultant particle velocity field (bottom) illustrates the important role of EO on particle transport in the fluidic cell.

ARTICLE INFO

Keywords:
Electrokinetics
Electro-osmosis
Electrophoresis
Nonpolar solvents
Surfactant
Astigmatism micro-particle tracking velocimetry
Electronic paper display
Colloids

ABSTRACT

Hypothesis: Electronic paper displays rely on electrokinetic effects in nonpolar solvents to drive the displacement of colloidal particles within a fluidic cell. While Electrophoresis (EP) is a well-established and frequently employed phenomenon, electro-osmosis (EO), which drives fluid flow along charged solid surfaces, has not been studied as extensively. We hypothesize that by exploiting the interplay between these effects, an enhanced particle transport can be achieved.

Experiments: In this study, we experimentally investigate the combined effects of EP and EO for colloidal particles in non-polar solvents, driven by an electric field. We use astigmatism micro-particle tracking velocimetry (A-μPTV) to measure the motion of charged particles within model fluidic cells. Using a simple approach that relies on basic fluid flow properties we extract the contributions due to EP and EO, finding that EO contributes significantly to particle transport. The validity of our approach is confirmed by measurements on particles with different magnitudes of charge, and by comparison to numerical simulations.

* Corresponding author.
E-mail address: H.M.Wyss@tue.nl (H.M. Wyss).

https://doi.org/10.1016/j.jcis.2024.02.194
Received 17 April 2023; Received in revised form 25 February 2024; Accepted 27 February 2024
Available online 7 March 2024

Findings: We find that EO flows can play a dominant role in the transport of particles in electrokinetic display devices. This can be exploited to speed up particle transport, potentially yielding displays with significantly faster switching times.

1. Introduction

Electrokinetic effects such as electrophoresis, electro-osmosis and dielectrophoresis are used to drive fluid and particle motion in fluidic systems, in applications such as microelectromechanical systems (MEMS) [1], point-of-care diagnostics [2] and display technologies [3]. In particular, these effects are the most established and promising way of realizing electronic paper displays, enabling low power consumption, wide viewing angle, and good outdoor readability. Conventional electrophoretic displays based on electrokinetic effects are based on the controlled movement of charged pigment particles dispersed in a nonpolar liquid to which a surfactant is added. The surfactant molecules form inverse micelles, which act as charging agents [4] within the nonpolar liquid, inducing a surface charge on the particles and cell surfaces, and act to stabilize the particles in the dispersion. Since these displays employ electrophoresis to transport charged particles, the electrophoretic mobility of the particles limits the switching speed of these electrophoretic displays. As a potential solution to this limitation, we here propose a display principle based on the concerted action of electrophoresis and electro-osmosis in nonpolar solvents.

In order for electro-osmosis to generate an electro-osmotic flow (EOF) along solid surfaces, these surfaces need to exhibit a net charge. The charged surface attracts counter-charge carriers and repels co-charge carriers, resulting in the formation of an electric double layer (EDL). The EDL thus has a net charge, as it contains an excess of counter-charge carriers. EOF occurs when an external tangential electric field is applied, driving this charged fluid layer to flow along the surface. Due to the tunable nature of the process, which is controlled by both the surface properties and the applied electric field, electro-osmosis has great potential for the precise and efficient actuation and manipulation of micro-flows and has found successful applications in micro-pumping [5] and micromixing [6,7].

In polar solvents like water, dissolved electrolytes (e.g. NaCl) easily dissociate to form ions, the presence of which is essential for electro-osmosis. In contrast, for weakly polar solvents, due to their low dielectric constant and the resultant high electrostatic energy barrier for charge separation, free charges are difficult to create. This results in surface charge densities that can be orders of magnitude lower than those found in aqueous systems. However, this situation can be ameliorated by adding surfactant molecules into the solvent, which form inverse micelles that can act as charge carriers in these systems (charged inverse micelles, CIMs); these surfactant molecules also assemble on surfaces, which enables the development of significant surface charges, comparable to those found in aqueous systems. The addition of surfactant molecules to nonpolar liquids therefore often leads to considerable charge-induced effects such as increased electrical conductivity and particle stabilization [8]. An electrical current between electrodes in these systems can develop by a migration of charged inverse micelles and a transfer of electrons between the electrodes and nearby charged inverse micelles [9]. Particle stabilization is the result of the formation of an electrical double layer, with a charged particle surface and a screening layer in the fluid that contains an excess of oppositely charged micelles. We would therefore expect that the addition of surfactants will also enhance the effects of EOF by an equivalent build-up of surface charge on the solid surfaces that form the boundaries of the fluid domain.

Both electro-osmosis and electrophoresis have been studied extensively in aqueous systems and, to a lesser degree, in nonpolar solvents [10]. While both these effects are well understood, they have generally been studied separately; electro-osmotic flow is often studied experimentally in systems that do not contain particles, while studies of electrophoresis generally use a parallel plates geometry, in which electro-osmotic flow does not play a significant role. However, in fluidic cell geometries beyond parallel plates, where EO is expected to play a more important role, the combined effects of EP and EO have not been studied in detail.

A better understanding of the interplay between these two physical effects could be beneficial for electronic paper display technologies, as it could potentially be exploited to drive a faster transport of particles from one electrode to the other, across a fluidic cell. In order to obtain a more complete understanding of the interplay of EP and EO in the transport of particles in nonpolar solvents, in-depth experimental studies on the three-dimensional (3D) flow of these particles are thus essential.

In this paper, we report on experiments in fluidic cells aimed at electrokinetic display technology that study in detail the electrokinetic motion of particles in nonpolar solvents, thus providing a detailed picture of the combined effects of electrophoresis and electro-osmosis on particle transport within these fluidic cells.

We do so by implementing an experimental model system and experimental setup based on 3D astigmatism micro-particle tracking velocimetry (A-μPTV) [11,12] that enables us to systematically study the three-dimensional trajectories of particles in nonpolar solvents contained within fluidic cells, as used in electrokinetic displays. While we cannot directly measure the fluid motion, by using 3D astigmatism micro-particle tracking velocimetry (A-μPTV) we are able to directly follow the three-dimensional trajectories of particles, and rationalize the observed behavior as the result of a combination of electro-osmotic flow of the liquid and electrophoretic migration of particles relative to that liquid.

Our experiments show that in addition to the conventional electrophoretic transport, electro-osmotic flows can significantly contribute to the overall particle motion. The electrode arrangement used in our experiments cannot directly be applied to an electrokinetic display. However, the electrode scheme used here should be directly applicable at the pixel level to an electrokinetic display employing lateral particle displacements.

More generally, the use of appropriate cell geometries and surface properties could open up the possibility to exploit electro-osmotic effects combined with optimized cell geometries for more efficiently driving particle displacement in electrokinetic devices, enabling faster switching in displays.

2. Materials and methods

2.1. Sample preparation

In our experiments, dodecane (n-Dodecane, ≥ 99%, Thermo Scientific^{TM}) is chosen as the nonpolar solvent. We use two different types of red Fluorescent polystyrene (PS) particles (2.5 wt% solid, Micro Particles GmbH, Germany) and (1 wt% solid, FluoroMax, Duke scientific corp and Distrilab, R0200) with a diameter of 2 μm. These fluorescent particles are dispersed in water; hence for our application we need to transfer these PS particles from an aqueous environment into dodecane solutions. To perform this solvent swap procedure, the aqueous suspensions are first dried in an oven at 80 °C for a total of 3-5 hours. In the final hours of the drying procedure, the samples are taken out of the oven several times and weighed on a precision balance to ensure a full evaporation of the water phase has been achieved. The samples are

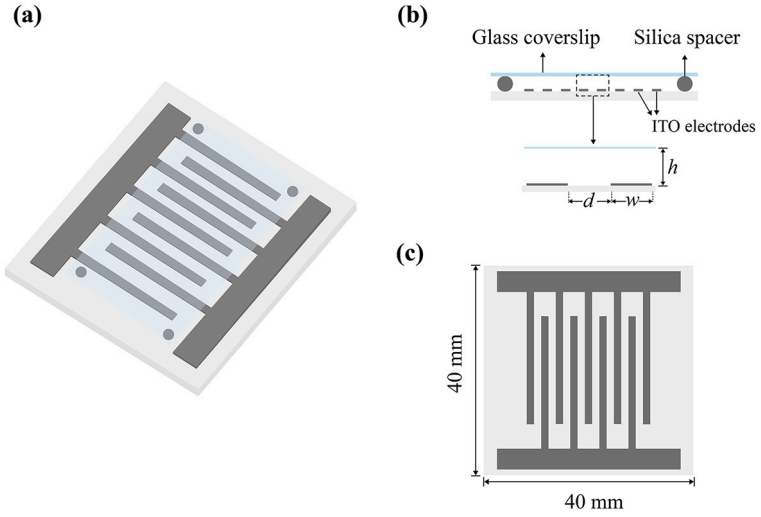

Fig. 1. Schematic of indium tin oxide (ITO) electrode patterns used in experiments. **(a)** Top view of glass substrate with ITO electrode patterns, the bottom surface of the fluidic cell. **(b)** Side view of fluidic cell. **(c)** Top view of the electrode pattern; the width of the electrode is $w = 200$ μm and the gap between electrodes is $d = 200$ μm.

then resuspended in dodecane and placed in an ultrasonic bath (Branson 2510 ultrasonic cleaner, USA) for a duration of 1 hour in order to break up particle clusters that have formed during the drying process.

After this, we add 1 wt% of OLOA 11k as a surfactant (the addition of a surfactant to these systems can facilitate charge separation, thus leading to an increased concentration of charge carriers in the solvent and to surface charges on the colloidal particles) to the solution. Finally, to further break up particle clusters that may remain in the system, we again place the sample in an ultrasonic bath, with bottles submerged in deionized water to approximately 2/3 of the height, for two hours.

We characterize the charging behavior of these particles in our dodecane solutions at a surfactant concentration of 1 wt% using the Litesizer^{TM} 500 (Anton Paar GmbH, Austria). This instrument measures the electrophoretic mobility of particles by applying an electric field and measuring the resulting motion of the particles using light scattering. This enables extraction of several important parameters such as the particle size and the Zeta potential, which is the electrical potential near the particle surface at the slip plane between mobile fluid and immobile near-surface fluid. For the particles from Microparticles GmbH we measure a Zeta potential of $\zeta = -82 \pm 5$ mV and for the FluoroMax particles purchased from Distrilab we find $\zeta = -42 \pm 4$ mV; the deviations indicate the standard deviation for 4 independent measurements on each type of particle. As a consequence, in the following we refer to the Microparticles GmbH particles and the FluoroMax particles as “higher-charge” and “lower-charge” particles, respectively.

We note that other methods for characterizing the particle charge, such as particle interaction measurements obtained in a quasi-2D geometry, or direct electrophoretic measurements inside a plate-plate electrophoretic cell, could yield a slightly different magnitude of the Zeta potential. However, for all methods we find a higher Zeta potential for the “higher charge” than for the “lower charge” particles. Such more detailed measurements and a comparison between the different characterization methods will be discussed in an upcoming publication.

2.2. Fabrication of fluidic cells

In our main experiments we use a micro-device with an interdigitated coplanar symmetric Indium-Tin-Oxide (ITO) electrode pattern, which is relevant to the operation of electrophoretic displays based on lateral particle displacement, as shown schematically in Fig. 1. The width of each electrode is 200 μm and the gap between them is 200 μm.

To fabricate the electrodes on the glass substrate we employ standard photolithography techniques, using the following protocol: First, we cut an ITO-coated glass substrate into a size of length × width = 40 mm x 40 mm. We spin-coat the ITO glass plate with a layer of a negative photoresist (SU-8) at 3000 RPM for 30 sec. After a pre-bake at 65 °C for 2 minutes, the mask with the designed pattern is aligned on the glass plate. We expose the masked glass plate under UV light at an intensity of 12.4 mW/cm^2 for 30 seconds. Then we apply a post-exposure bake treatment on a hot-plate at 95 °C for 6 minutes. Subsequently, we put the exposed glass plate into the developer solution (mr-Dev 600) for 5 minutes, where the unexposed photoresist is dissolved. The ITO layer with the desired pattern is then created by removing the undesired regions through etching in an etchant solution (HCL: H_2O: HNO_3 = 4: 2: 1 by volume) for 10 minutes, rinsing at least 3 times with DI water, and finally blow-drying with N_2. We measure the electrical resistance between the different patterned electrodes to check whether the patterns have been formed correctly, without residual electrical connections between the separate electrodes. If the electrical resistance were too low (we aim for a measured value of more than 6 MΩ), this would indicate a defect in the electrode geometry or an insufficient removal of ITO between the electrodes. In this case we would repeat the procedure of ITO etching until the electrical resistance is appropriate. Finally, after achieving the desired electrode pattern, we place the glass plate into a solution of Remover-PG (MicroChem) to remove the photoresist.

We use this finished glass slide with ITO electrode pattern to construct our fluidic cell, where the ITO substrate serves as the bottom wall. For the top wall we use a bare silica slide of 24 mm x 24 mm surface area and thickness 400 μm. To obtain a cell with a uniform and well-defined gap between the top and bottom glass surfaces, we employ uniformly sized silica particles of 30 μm diameter (Suzhou Nanomicro Technology Co., Ltd, Suzhou, China), mixed with a UV-curable glue (Norland Optical Adhesive 81 (NOA81)), as spacers. To construct the sample cell, a small drop of this glue with incorporated spacer particles is applied to each of the 4 edges of the top glass plate using a precision glue dispenser (ShenZhen Kuaiqu electronic Co., Ltd, China), after which the top glass slide is carefully placed onto the bottom substrate. After applying pressure to ensure contact of the spacer particles with the top and the bottom substrate, the glue is cured by illumination with a UV-LED exposure system (IDONUS, UV-EXP 150R, Neuchatel, Switzerland) with an intensity set to 15 mW/cm^2 for a duration of 50 s.

2.3. Astigmatism micro-particle tracking velocimetry

Astigmatism micro-Particle Tracking Velocimetry (A-μPTV) is a single camera measurement technique to determine the three dimensional

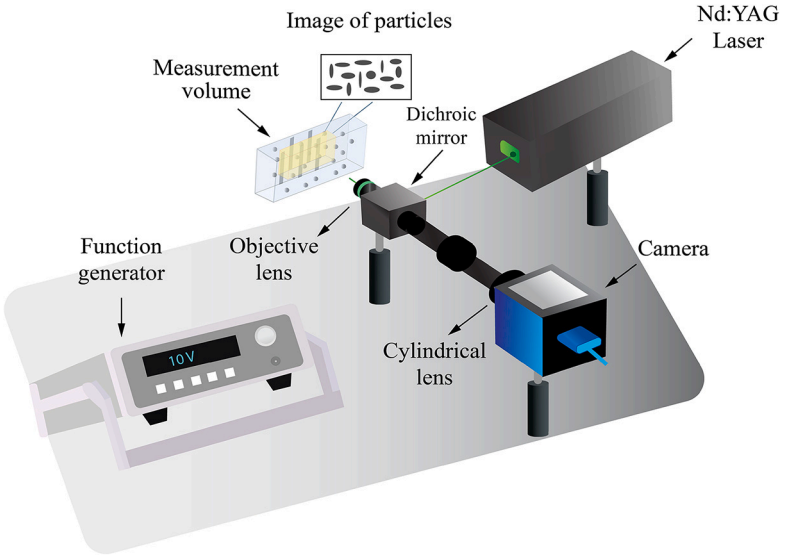

Fig. 2. Schematic of the experimental setup used in our astigmatism micro particle tracking velocimetry (A-μPTV) experiments.

displacement of particles. A-μPTV system makes use of a cylindrical lens in the optical path, which introduces an astigmatism in the optical system. This implies that the focal distance is different in the vertical and the horizontal direction, as the cylindrical lens acts as a lens only in one of these two orthogonal directions. This astigmatism leads to an apparent elliptical shape of spherical fluorescent particles on the captured image, where the aspect ratio and orientation of the ellipse depends on the z-axis coordinate of each particle. Based on this elliptical shape, we can thus identify the full three-dimensional positions of the particles within the sample cell. Further, based on these measured particle positions in each frame of a captured microscope video sequence, we calculate the velocity field by means of a tracking algorithm. Fig. 2 depicts a configuration of the A-μPTV system used in the present study. By using the full numerical aperture of one single microscope objective, A-μPTV has a large range of measurable depth, and is suitable for complex flows with limited optical access compared to multi-camera techniques.

2.4. Measurement setup

We use a function generator (33120A Function / Arbitrary Waveform Generator) to provide a voltage signal to the electrode arrays through the contact pads of the device. To amplify the output voltage from our function generator, a voltage amplifier (WMA-100A, Falco) is employed. In our main measurements, we choose to apply a peak-to-peak voltage of 20 V (+10 V on one electrode and −10 V on the other electrode), where the polarity of the voltage is switched every 16.67 s, resulting in the transport of particles towards the opposite electrode. For all conditions studied here, we find that this allows ample time for all particles to travel across the fluidic cell. We choose the value of 20 V as it is at the high end of voltages compatible with commercially available display driving devices. We have also performed simpler experiments to study the average transport velocity of particles across a fluidic cell as a function of applied voltage, shown in the supplementary information, section 5. These results indicate that above an applied voltage of around 20 V the particle velocity no longer increases linearly with the applied voltage. Moreover, at higher applied voltages, due to increased particle velocities, in particular near the electrodes, it becomes increasingly difficult to accurately track our particles using our astigmatism micro-particle tracking setup. We therefore use a voltage magnitude of 20 V in all our main experiments.

We perform three-dimensional particle tracking measurements using the astigmatism micro-particle tracking velocimetry (A-μPTV) technique. In these measurements, a fluorescence microscope with a 20× Olympus objective lens (Numerical aperture of 0.45, focal length of 7:9 mm and variable cover correction from 0 to 2 mm via correction collar) is employed to observe the charged particles. To illuminate the fluorescent particles, a Nd:YAG laser generation (ICE450, Quantel, USA) is used to produce a pulsed monochromatic laser beam with a wavelength of 532 nm and an energy of 200 mJ per pulse (the time interval of each laser pulse is 6 ns). The light emitted by the illuminated fluorescent particles has a wavelength of 612 nm. A digital imaging source camera (DFK 33UX252, Germany) records the particle images, with a resolution of 1980×1080 pixel^2. To induce the astigmatism required for A-μPTV, a cylindrical lens with a focal length of 150 mm (LJ1629RM-A, Thorlabs, USA) is incorporated into the optical path. A digital delay generator (DG535, Stanford Research Systems, USA) simultaneously controls the timing of the laser and the camera.

2.5. Image processing

To extract the full three-dimensional positions of the particles, we employ a custom Matlab code that extracts the xy-position as well as the apparent elliptical shape of each particle, from which the corresponding z-positions are calculated, Fig. 3 shows all steps of the image processing. In a first step, to remove pixel-to-pixel noise, the original images are smoothed by a real-space bandpass filter.

By identifying local maxima in the smoothed images that lie above a chosen threshold in intensity and then calculating the centroid of bright spots to sub-pixel accuracy, we obtain a rough estimate of the x- and y-positions of the detected particle [13]. Based on the initial positions of the detected particle center, a detection region with 240×150 $pixel^2$ is chosen from the processed frame to estimate the z-position (the detection region should be set large enough to cover the full image of a single particle). We then apply a bi-cubic spline interpolation on each detection region to improve the resolution of the particle image. To calculate the image deformation of each particle, the detection region is then converted into black and white (B&W), according to a gray level threshold that is based on a histogram of the image intensity in the detection region. Based on the B&W image, the boundary of each particle image is established, and the corresponding length of major and minor axes of the elliptical particle images are measured in the x- and y-directions [12].

Finally, in order to be able to extract the z-positions of particles, we perform a calibration of the z-component by linking the deformation of the apparent particle shape in the xy-plane to its relative z-position with respect to the two focal planes. To do so, we choose several particles that are fixed to the bottom of the channel as reference particles.

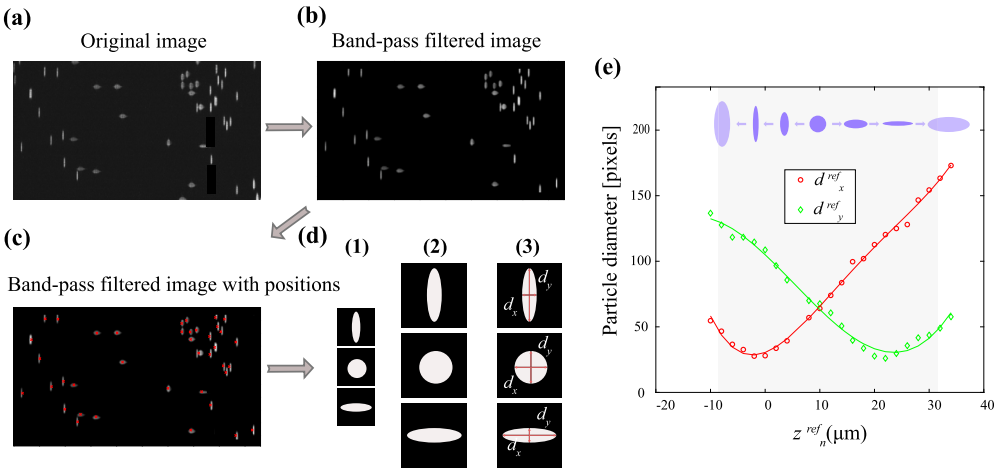

Fig. 3. Image processing to evaluate particle diameters. Steps for digital image analysis: **(a)** Original image. **(b)** Band-pass filtered image. **(c)** Determination of the center of particles. **(d)** (1) Based on the primary positions of the detected particle center, a detection region is defined. (2) Then a bicubic spline interpolation is applied on each detection region, to improve the resolution of the particle image. (3) Finally, to quantify the apparent shape of each particle, the detection region is converted into black and white, and the corresponding diameters of the particle images are measured in the x- and y-directions. **(e)** Calibration curve. The width $d^{\mathrm{ref}}_{n,x}$ and the height $d^{\mathrm{ref}}_{n,y}$ as a function of the reference z-position for the case of a 2 μm diameter particle. The calibration range is shown by the highlighted gray area. (For interpretation of the colors in the figure(s), the reader is referred to the web version of this article.)

We displace the bottom plane along the z-direction of the optical system, with steps of 2 μm, then we measure the average diameters of the reference particles image $d^{\mathrm{ref}}_{n,x}$ and $d^{\mathrm{ref}}_{n,y}$ in the x- and y-directions corresponding to the z-positions (z^{ref}_n [μm]), where n is the number of the displacement steps. The result is shown in Fig. 3(e). In order to obtain smooth calibration functions averaged over the whole set of calibration data, we use fourth order polynomial fits to the measured calibration points $d^{\mathrm{ref}}_{n,x}$ and $d^{\mathrm{ref}}_{n,y}$ to z^{ref}_n, shown in Fig. 3(e) as red circles and green diamonds, respectively; the resultant calibration functions $d^{\mathrm{cal}}_x(z)$ and $d^{\mathrm{cal}}_y(z)$ are shown as a red and green solid line.

We determine the z-positions of particles in the experiment by a least-squares fit to minimize the deviation between the measured particle diameters and those obtained from the z-dependent calibration functions of the particle diameters between the experimental measurement and the calibration functions as

$$\mathrm{Dev}(z) = \sqrt{\left(d_x - d^{\mathrm{cal}}_x(z)\right)^2 + \left(d_y - d^{\mathrm{cal}}_y(z)\right)^2}, \tag{1}$$

where d_x and d_y are the apparent diameters of the particle in the x- and y-directions, respectively.

For $\min(\mathrm{Dev}(z)) < 3$ pixels, we consider the particle image to be valid, and extract the corresponding z-value as the estimated relative z-position z_{app}. Note that the particle image intensity restricts the accuracy of the estimated z-position of the detected particle. The detected intensity of the particle image decreases when it is far away from the two focal planes. The calibration range, the region where the z-position can be reliably detected, is therefore dependent on both the fluorescence activity of the particles and the cylindrical lens, which determines the distance between the two focal planes.

In this study, the calibration range is around 40 μm (see the calibration curve in Fig. 3(e)). Correspondingly, the uncertainty on the estimated z-position according to the reference z-position is calculated as

$$\epsilon^z_{\mathrm{dev}} = \frac{1}{N}\sqrt{\sum_{n=1}^{N}\left(z^{\mathrm{ref}}_n - z_{\mathrm{app}}\left(d^{\mathrm{ref}}_{n,x}, d^{\mathrm{ref}}_{n,y}\right)\right)^2}, \tag{2}$$

and is about 0.098 μm.

To extract correct z-positions from our experiments, it is important to note that during the actual experiments the dodecane level above a tracer particle depends on the particle's z-position in the channel. This is different from the situation during calibration, where we moved the sample holder and always imaged a particle stuck to the top or bottom surface of the fluidic cell; the thickness of the dodecane layer above the tracer particle was thus fixed in these calibration measurements. If we use the relationship between z-position and particle shape as established during calibration, due to the difference in refractive index between the dodecane and air, we thus obtain an apparent z-position of the tracer particle, z_{app}, that is different from the actual position z_{act}. We can correct for this and express the actual z-position as a function of the apparent position as

$$z_{\mathrm{act}} = z_{\mathrm{app}} \cdot \left(n_{\mathrm{dodecane}}/n_{\mathrm{air}}\right), \tag{3}$$

where $n_{dodecane} = 1.421$ is the refractive index of dodecane and $n_{air} = 1$ the refractive index of air. Accordingly, in the example shown (Fig. 3(e)), the actual depth of the measurable volume is corrected to about 57 μm.

3. Results and discussion

3.1. 3D particle trajectories

Fig. 4 shows an example of typical 3D trajectories of charged particles within the fluidic cell at a peak-to-peak voltage (V_{PP}) of 20 Volts, where the displacements of the negatively charged particles are tracked as a function of time with a delay time of 0.05 s. After extracting the 3D positions (x, y and z) of the particles (using the A-μPTV technique) based on the positions in consecutive frames, we calculate the three components of the particle velocity (u_x, u_y and u_z). A side view of particle trajectories is given in Fig. 4(b) for clarity, where the x-component of particle velocity is calculated at each position and shown in colors.

We observe that the charged particles follow different paths depending on both their initial position on the electrodes and their charge (it is reasonable to assume that particles don't all have exactly the same charge). If the particles are initially near the edge of the electrode and have a higher charge, their subsequent trajectory will essentially follow the electric field lines, as electrophoretic motion dominates. However, particles with lower charge, and/or starting further away from the electrode edge, where the electric field is lower, will predominantly follow the fluid motion. We indeed observe that these particles move away from the electrode edge, towards the center of the electrode.

Note that some of the particle trajectories displayed in Fig. 4 only cover a limited number of consecutive time steps. This is because in

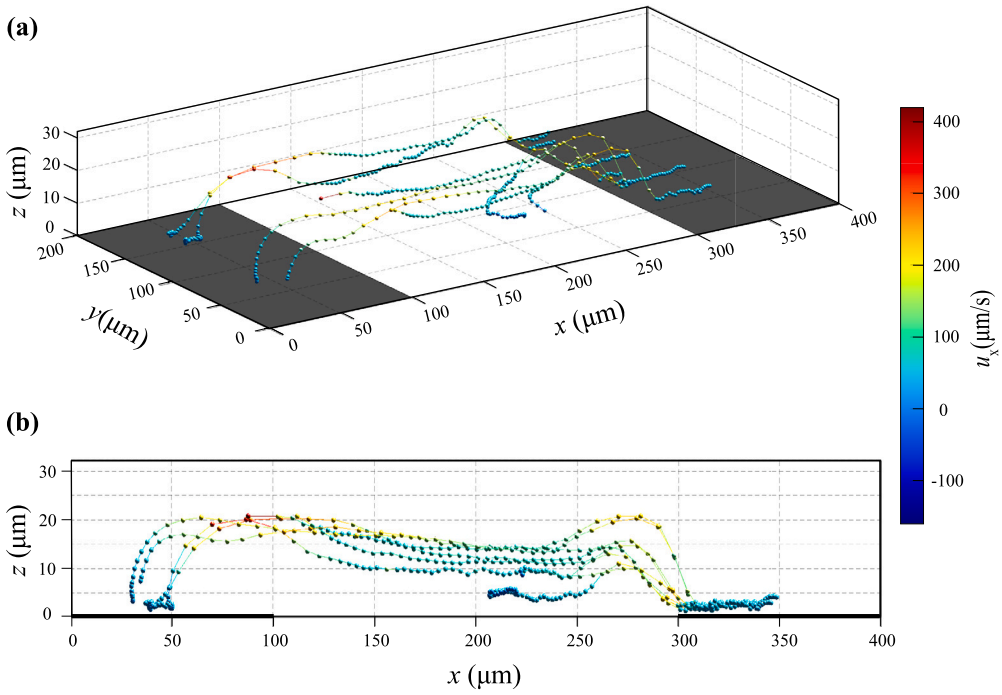

Fig. 4. (a) 3D trajectories of several charged particles in a fluidic cell acquired by A-μPTV (voltage: 20 V peak–to-peak (V_{pp})). The displacements of the particles are tracked with a delay time of 0.05 s. The starting position of the particles is on the left electrode. **(b)** Side view of particle trajectories. The electrode positions are indicated as dark areas. The sphere colors represent only the x-component u_x of the particle velocity, with magnitudes indicated by the color bar.

some frames particles may be too close together in the (x,y)-plane, or particles may leave the imaged field of view, such that their position cannot be detected in all frames and a full trajectory cannot be constructed.

As seen from the color labeling in Fig. 4, along each trajectory, the magnitude u_x of the x-component of the velocity first reaches a peak near the electrode edge, then decreases with distance from the edge along the channel, and finally increases again close to the other electrode edge.

3.2. Velocity field

Our A-μPTV measurements yield the three-dimensional trajectories of particles within our chosen field of view. In order to better visualize and analyze the flow of particles, we wish to extract a velocity field for the particles from the measured particle positions. To do so, with the knowledge of 3D positions of particles, we match the particle positions in consecutive frames by using a nearest-neighbor approach [14], where possible positions in the next frame are limited to a cut-off radius from a particle's position in the previous frame. Using the obtained particle trajectories we obtain for each particle trajectory a velocity vector between two consecutive frames. From this collection of velocity vectors we can then obtain a particle velocity field by averaging and interpolating all these measured individual velocity vectors.

In doing so, to improve statistics we repeat the experiments for several full cycles and then we combine the velocity vectors obtained within the first 10 s after the polarity of the voltage is switched (the polarity is switched every 16.67 seconds) into a single data set that describes the flow field in the microchannel. The y-component u_y of the velocity field of most particles remains small everywhere. For the average velocity in the y-direction we find $\overline{u_y} \sim 2.06$ μm/s, as opposed to the x-direction, where we find $\overline{u_x} \sim 23.7$ μm/s. For the magnitudes in the y- and x-directions we find $\overline{|u_y|} \sim 12.6$ μm/s and $\overline{|u_x|} \sim 51$ μm/s, respectively. This suggests that the flow of particles can be approximated as a quasi-two-dimensional (quasi-2D) flow. Therefore, in visualizations of the flow field we here neglect the y-dimension and present the measured 3D particle velocities only within the (x,z) plane.

To further smooth our data, we filter out the obvious outliers in the retained data and then use the remaining raw velocity vectors to obtain interpolated values on a Cartesian grid with spacing $\Delta x = 4$ μm and $\Delta z = 1$ μm. We obtain the interpolated values $\overline{\boldsymbol{u}}(x_i, z_i)$ for each point on this grid by using a Gaussian-weighted averaging algorithm [15], as

$$\overline{\boldsymbol{u}}\left(x_i, z_i\right) = \sum_{j=1}^{N} w'_{i,j} \boldsymbol{u}\left(x_j, z_j\right) , \tag{4}$$

where $w'_{i,j}$ is the normalized weight of the neighboring particles, depending on the distance from each neighboring particle j to the point i on the grid as

$$w'_{i,j} = \frac{w_{i,j}}{\sum_{j=1}^{N} w_{i,j}} , \tag{5}$$

with

$$w_{i,j} = \exp\left(-\frac{\left(x_i - x_j\right)^2 + \left(z_i - z_j\right)^2}{\sigma_d^2}\right) , \tag{6}$$

where (x_j,z_j) are the coordinates of the neighboring particle j, (x_i,z_i) the coordinates of the grid point i, and σ_d is the characteristic length scale for the Gaussian averaging. The choice of σ_d thus determines the range over which the velocity values are averaged; large values result in an over-smoothed velocity field, whereas very small values generally yield more fluctuations in the resulting velocity field, as in this case each velocity value is dominated by the velocity of only the closest neighboring particle, rather than being averaged over many neighbors.

Using a value for σ_d that is compatible with the typical distance between the raw velocity data points, we obtain an appropriately averaged velocity field, such as the example shown in Fig. 5. This velocity field is obtained in an array of interdigitated symmetric electrodes at a peak to peak voltage of 20 V_{PP} applied for a duration of 10 s on a sample of fluorescent polymer micro-particles with a diameter of $dp = 2$ μm

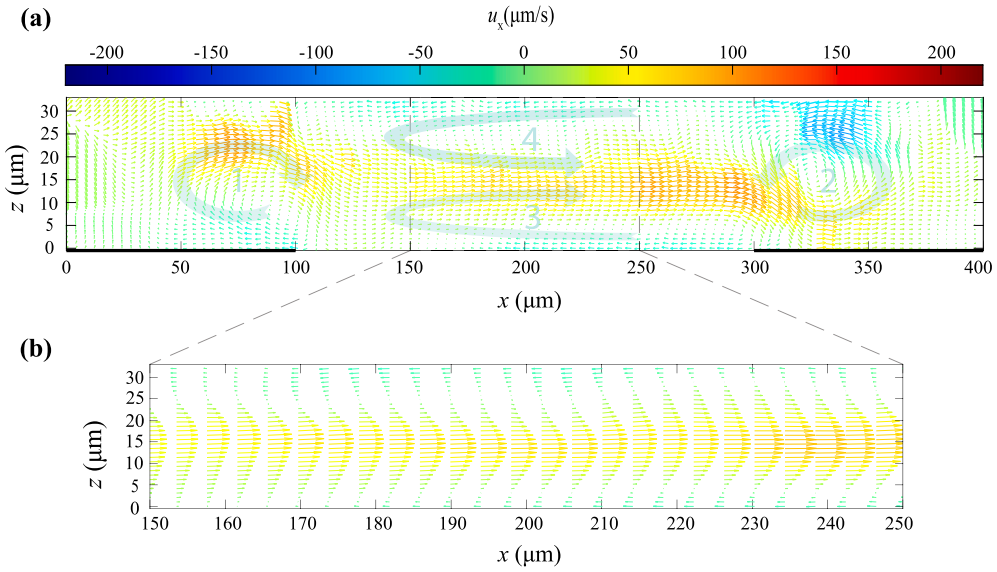

Fig. 5. (a) Particle velocity vectors at an applied peak-to-peak voltage of 20 V acquired during 10 s after switching the polarity of the voltage. The arrows reflect the magnitude and direction of the velocity (note however that the scaling is different along the two axes). The arrow colors represent only the x-component u_x of the velocity, with magnitudes indicated by the color map shown on top. The positions of the electrodes are indicated by black solid lines; the dashed lines indicate an area of interest in the middle between the two electrodes, where we further inspect the velocity field. The observed four main flow vortices are indicated as thick arrows numbered 1 to 4. **(b)** The velocity profile of charged particles in the middle of the microchannel as a function of height, averaged over all available velocity data over a duration of 10 seconds. We show the velocity field within the region of interest.

(Fluoro-Max, Duke Scientific Corp) in a 2 wt% solution of OLOA 11k surfactant. For the interpolation procedure, we used $\sigma_d = 3$ μm, which we find to yield a good compromise between oversmoothing (σ_d too large) and enhancing local point-to-point fluctuations (σ_d too small). Note that the observed fluctuations of measured velocity vectors vary significantly for different locations within the sample cell, as illustrated by a quantification of data quality of measured velocity vectors shown in the SI, section 1.

A typical example of the flow structure that arises due to the combined effects of electro-osmosis and electrophoresis is shown in Fig. 5(a), where the arrows reflect the magnitude and direction of the velocity field. To emphasize the vortex structure we choose the arrow colors to represent only the x-component u_x of the velocity, with magnitudes indicated by the color map shown on top.

We observe a clear pattern of regions with positive and negative values of u_x, reflecting a motion of particles towards the right and the left side of the cell, respectively. Studying these patterns further, we observe that the flow field exhibits two clockwise (CW) and counterclockwise (CCW) rotations above the electrodes, and along the channel due to electro-osmotic effects. These vortices are indicated schematically in Fig. 5(a) as thick arrows numbered 1 to 4. They can be understood by describing the induced electric field in the geometry with co-plane ITO electrodes, and negatively charged glass surface filled with micelles. In the presence of an external electric field, a tangential component of electric force is exerted on the mobile counter-charged micelles in the electrode double layer creating an electro-osmotic flow parallel to the electrodes, which results in fluid flowing from the edge towards the center of the electrodes. A single vortex thus forms in the region between the edge and the center of each electrode (vortex 1 and 2 in Fig. 5(a)).

Similarly, since the glass surface is negatively charged, the positively charged micelles accumulate near the bottom and top surfaces. By applying a voltage (in this case the electric field is from right to left) the positively charged micelles in the diffuse double layer move along the direction of the tangential component of the electric field (from right to left), with the corresponding backflows flowing in the opposite direction in the center of the sample cell. This leads to an enhanced flow in the middle of the microchannel that yields a faster transport of particles from left to right in this region. The corresponding vortices are indicated as vortex 3 and 4 in Fig. 5(a).

Extracting velocity fields during the time period where the polarity of the applied voltage is switched, we observe an overall similar pattern, as shown in the SI, section 2. As expected, the directions of velocity vectors are opposite in the central region of the fluidic cell (vortices 3 and 4). However, the vortices above the electrodes (vortex 1 and 2), maintain the same directions for both polarities of applied voltage.

3.3. Velocity profile near the center of the fluidic cell

To further quantify our results we focus our attention on the velocity profile of charged particles near the middle of the fluidic cell averaged over the first 10 seconds after a voltage is applied (see Fig. 5(b)). In this region, the velocity field is relatively uniform along the x-direction, and does not appear to fluctuate significantly over time; therefore we are able to obtain higher quality velocity data in this area. In contrast, near the electrode edges, the observed vortex patterns can fluctuate significantly over time, which means that averaging over time tends to yield inaccurate and/or smeared out velocity field data. Near the center of the flow cell, we do not observe such fluctuations of the flow pattern and the particle velocities are directed overwhelmingly along the x-axis direction. To more clearly visualize the flow field we highlight the x-component of the velocity field in colors, with positive velocities shown in red tones and negative velocities in blue tones, according to the color map shown on top of the main graph in Fig. 5. In this figure we can clearly identify two back flows near the bottom and top of the microchannel which we attribute to electro-osmotic effects. Since both top and bottom glasses are negatively charged, the fluid near these interfaces comprises an excess of positive charge carriers, and by applying an electric field these charge carriers move in the direction of the electric field, which in this case points from the right to the left side, thus inducing two reverse flows. The magnitude of these two flows depends on the zeta potential of the glass surfaces, a measure of the magnitude of their surface charge when in contact with the solvent.

These backflows thus contribute directly to a faster migration of particles in the middle of the cell moving from left to right, with electrophoretic migration acting in the same direction. Thus, even as the

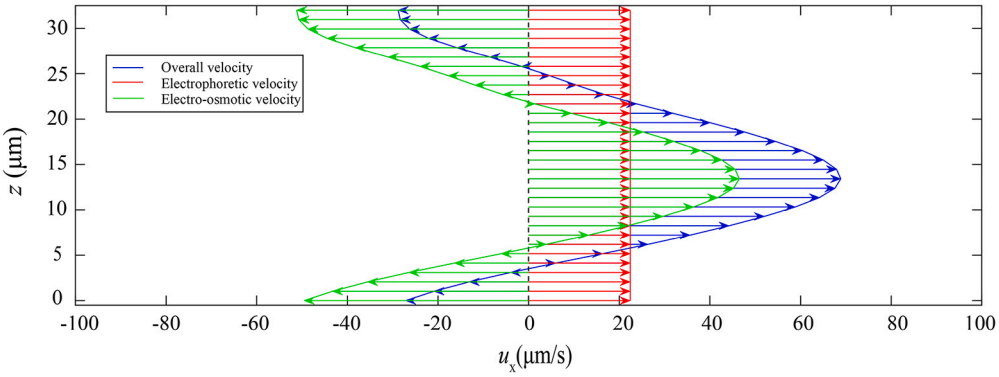

Fig. 6. Example of the separation of the overall velocity (blue), into electrophoretic (red) and electro-osmotic (green) contributions. We note that the overall particle velocity profile $u_x(z)$ is the x-component of the particle velocity averaged over the entire central region of the fluidic cell shown in Fig. 5(b).

electro-osmotic flows are driven to flow from right to left, due to the incompressibility of the fluid for each of those flows a corresponding backflow must be induced near the middle of the cell. The combined effects of electrophoresis and electro-osmosis thus lead to high particle velocities in this region, with the maximum velocity reaching 70 μm/s at $z = 14.5$ μm where the two back flows maximally enhance the transport of charged particles.

3.4. Extracting information on EO and EP from velocity profiles

The velocity profiles near the middle of the channel can be used to extract valuable information on the electrophoretic and the electro-osmotic effects that govern our experiments. Indeed, we cannot directly measure the velocity field of the background liquid, which is driven by electro-osmosis. Instead we are always measuring the velocity field of the particles, which is due to the EO flow of the background liquid plus the electrophoretic velocity of the particles relative to that background liquid.

However, due to the relative simplicity of the flow situation near the middle of the channel, we can make several assumptions that enable us to separate the particle velocity field into a fluid flow (driven by electro-osmosis) and a migration of particles relative to the fluid (driven by electrophoresis). Firstly, we assume that the fluid flow in the (x,z)-plane is independent of the x-position of the particles, which means that we can treat all velocity data obtained in different x-positions within this region as equivalent; this is confirmed by a detailed analysis of flow profiles at different x-positions, shown in the SI, section 3. We further assume that there is no net flow over long distances in the x-direction, and that the fluid is incompressible. Regarding the electrophoretic effects we assume that the charge of the particles is uniform, i.e. that all particles carry the same charge. We further assume that near the middle of the channel, the electric field points along the x-axis and is uniform in magnitude. This assumption is supported by our computer modeling, in which near the middle of the sample cell we find a difference of only 1.7% between the electric field strength at the bottom and the top of the cell.

Under these assumptions, the integral of the x-component of the electro-osmotic fluid velocity over the height of the channel must be zero. We can make use of this property to decompose the measured overall velocity into electrophoretic and electro-osmotic components. To do so, we employ a velocity profile that is averaged in the x-direction over the entire middle region of the fluidic cell, encompassing all the data displayed in Fig. 5(b). This averaged overall particle velocity profile $u_x(z)$ is displayed as a blue line and arrows in Fig. 6. By calculating the integral of this curve over the height of the channel we can extract the electrophoretic velocity, shown as a red line and arrows in Fig. 6. The fluid flow (green curve and arrows), which originates from electro-osmotic flow, is then extracted by subtracting the electrophoretic velocity field from the overall particle velocity profile.

The result clearly shows that in addition to the conventional electrophoretic migration, electro-osmotic flow has a notable effect on particle displacements, which results in a significantly faster particle transport.

These findings are also in line with numerical simulations that we have performed for our system, shown in the SI, section 4, which exhibit the same overall flow patterns observed in our experiments, and also confirm the prominent role of electro-osmosis in driving particle transport. In our model, the fluid flow and transport of charge carriers within this fluid is modeled using a combination of the Poisson, Nernst-Planck, and Navier-Stokes equations, as described in section 4.2 in the supplementary information.

The effect of particle charge on the velocity field

Based on the theoretical expectation that the motion of the particles is determined by the sum of the contributions from the electro-osmotic flow of the background liquid and the electrophoretic migration of the particles relative to the background liquid, we expect that increasing the particle charge will lead to a decrease or even elimination of the reverse motion of charged particles near the bottom of the cell, as the electrophoretic migration in the forward direction would become dominant. To further test this physical picture, we perform experiments with two separate particle systems that exhibit different particle charges (as explained in section 2), keeping all other experimental parameters constant.

Indeed, we find these experiments to be consistent with our physical picture, as shown in Fig. 7(a) and 7(b), where we compare the velocity profiles of the two particle systems near the center of the cell. It is clearly observed that using particles with higher charge does enhance the electrophoretic migration of particles, which leads to an increase in the overall velocity of the charged particles. Along with this increased overall flow velocity, the back-flow near the top and bottom wall surfaces is nearly completely eliminated, as the electrophoretic velocity of the particles near the wall becomes comparable in magnitude to the velocity of the electro-osmotic flow that acts in the opposite direction.

In the middle of the cell, however, the fluid convection induced by electro-osmosis still leads to a significant increase of the particle flow velocities, as here the electro-osmotic and electrophoretic effects both lead to particle transport in the same direction.

To further compare the behaviors of particles with different charges, we again extract an averaged velocity profile in the middle of the channel as a function of height for both particle types. Note that, as seen in Fig. 7(a-b), in these experiments we lack data near the top surface of the fluidic cell, as not enough particle trajectories pass through the top layer region; our experimental data extends to a height of 25 μm and the height of the fluidic cell is ~32 μm. To obtain a velocity field over the full height of the fluidic cell, we assume that the velocity field is symmetrical with respect to the z-axis, which is justified by our experimental observations for all cases where we were able to obtain velocity

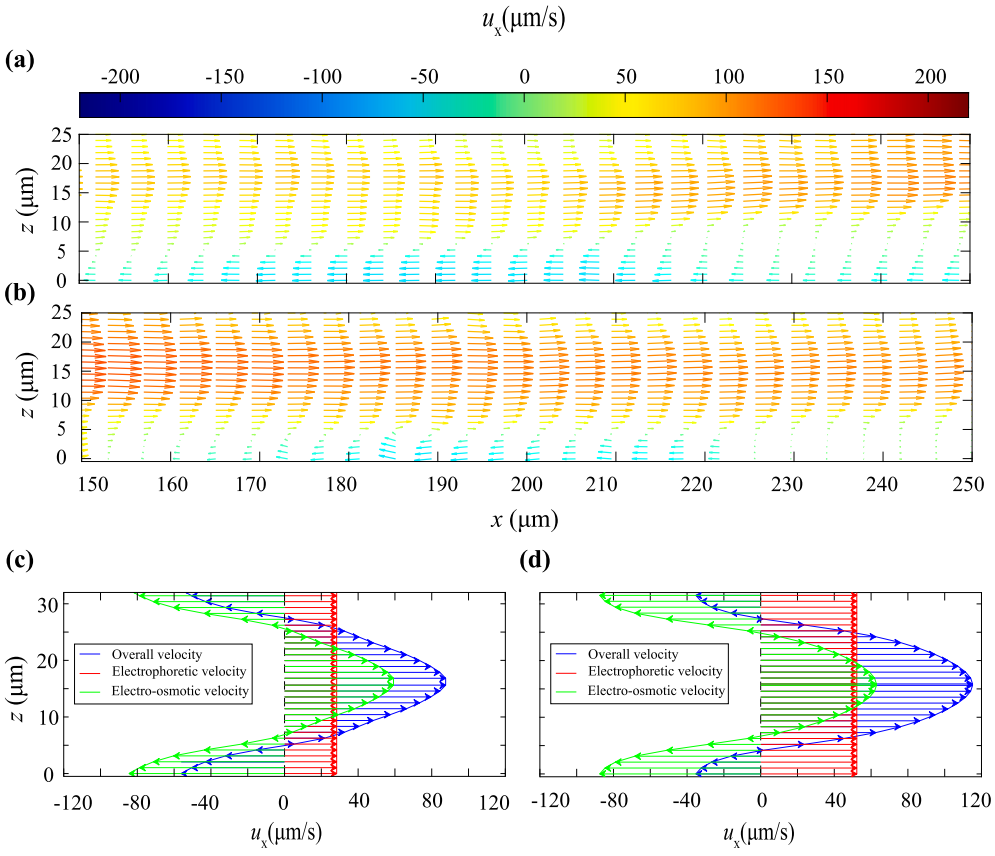

Fig. 7. The velocity profile of charged particles in the middle of the microchannel as a function of height, averaged over a duration of 10 seconds at an applied voltage of 20 V. **(a)** velocity profile for particles with lower charge. **(b)** velocity profile for particles with higher charge. The overall velocity (blue), obtained by averaging in the x-direction over the entire middle domain of the fluidic cell, is separated into electrophoretic (red) and electro-osmotic (green) contributions. **(c)** "lower charge" particles and **(d)** "higher charge" particles.

data over the full height of the cell, such as those shown in Fig. 5. Using a least squared error curve matching algorithm, matching the offset of a mirrored velocity function for optimal overlap with the original velocity data, we obtain a symmetric function for the z-dependent averaged velocity, spanning over the entire height of the sample cell.

To further compare the behaviors of particles with different charges, we plot the averaged velocity profile of the two particle types in the middle of the channel as a function of height, and we display the corresponding electro-osmotic, electrophoretic, and overall velocities separately with different colors (Fig. 7). After obtaining the overall velocity of particles from our 3D measurement, we again average the velocity of charged particles in the x-direction over the domain near the center of the fluidic cell, including all data shown in Fig. 7. These averaged overall particle velocity profiles $u_x(z)$ are indicated as blue lines and arrows in Fig. 7(c) and 7(d). Subsequently, we again integrate the velocity profile in the z-direction to obtain the net electrophoretic velocity (shown as red lines in Fig. 7). Subtracting this from the overall particle velocity profile yields the velocity profile of the background fluid, driven by electro-osmosis (green lines in Fig. 7).

As observed in Fig. 7, by using particles with higher charges the contribution of electrophoretic migration is indeed increased while fluid flow in both cases is comparable. The change in the electrophoretic velocity is remarkably good agreement with our Zeta potential measurements on these particles. We find an increase of the electrophoretic velocity by a factor of 1.85 from 28 μm/s to 52 μm/s from the "low charge" to the "high charge" particles, in good agreement with the ratio of 1.95 that we measure between the corresponding Zeta potentials of -42 ± 4 mV and -82 ± 5 mV, respectively.

4. Conclusions

We set up a model system and adapted optimized experimental techniques for studying the combined effects of electrophoresis and electro-osmosis acting on colloidal particles, surfactant and non-polar solvent under the influence of an applied electric field.

The 3D particle trajectories in a fluidic cell with an electric field generated by an array of interdigitated symmetric electrodes were acquired using astigmatism micro-particle tracking velocimetry (A-μPTV). From these particle trajectories we extracted a velocity field for the charged particles. We assumed that the 3D particle velocity field can be treated as a quasi-2D flow field since the y-component of the particle velocities was small everywhere and varied within a small range. Under these assumptions, we have shown that the velocity profile of charged particles in the middle of the channel can be used to extract information about the electrophoretic and electro-osmotic effects that govern our experiments. In agreement with a simple model of electrokinetics in our system, our experiments show that electro-osmosis contributes significantly to particle motion.

This opens up the possibility to systematically exploit electro-osmotic effects combined with optimized cell geometries for more efficiently driving particle displacement in electrokinetic devices.

To further validate our experimental approach, we carried out experiments using two separate particle systems with different particle charges, keeping all other experimental parameters constant. We observed that using particles with higher charge can boost the electrophoretic motion of particles, leading to an increase of the overall velocity of the charged particles. Importantly, we observed a nearly unchanged fluid velocity field between the two cases; this is expected,

Table 1
Comparison of effective mobility $\mu_{\text{eff.}}$ between our approach and traditional electrokinetic devices used in industry and described in publications and patents. From the typical distance d between the electrodes in the device, the typical applied voltage U, and the characteristic switching time scale τ, we obtain the typical velocity u of the particles, and finally the effective mobility, defined as $\mu_{\text{eff.}} = u \times \frac{d}{U}$.

Source	d [μm]	U [V]	τ [ms]	u [μm/s]	$\mu_{\text{eff.}}$ [μm^2/s V]
Typical EPDs [17]	40	94.4	100	400	169
Adv. Color E-Paper [18]	20-30	17-30	250-500	40-120	26-211
This work	~200	20	~2000	~100	~1000

as the electro-osmotic effects that drive fluid motion should not be affected by particle charge. This agreement validates both the experimental method used, as well as our simple method for extracting the EO and EP velocities from the measured overall particle velocity field.

The work presented here aims at emphasizing that electro-osmosis could be exploited for dramatically improving the performance of electrokinetic displays. As such, we have not yet performed a detailed study on how a variation of cell geometries, surface chemistries, or other parameters could be used for further optimizing the performance of the approach.

Nevertheless, to put our approach in perspective with the current state of the art, we perform a simple comparison to typical approaches used today in some of the most advanced electrokinetic displays. To make such a comparison, we focus on the effective mobility μ_{eff} of the particles within the device, which is the average transport velocity u of the particles from one electrode to the other, normalized by the ratio between the applied voltage U and the distance d between the electrodes, as $\mu_{\text{eff}} = u \times \frac{d}{U}$. It is important to note that this effective mobility is expected to be lower than the electrophoretic mobility of the particles themselves, which is defined as the ratio between the electrophoretic migration velocity and the electric field, as $\mu_{\text{p}} = u \times E$; due to the buildup of charge carriers at the electrodes and the resultant screening effects, the electric field within the bulk fluid is generally reduced, and thus $E < \frac{U}{d}$. In measuring the electrophoretic mobility of particles, for instance using electrophoretic light scattering, an oscillating voltage is generally applied at frequencies that are high enough to limit the buildup of charge carriers at the electrodes. Typical values for the electrophoretic mobility μ_{p} of particles used for electrophoretic displays in nonpolar solvents are generally in a range of 100–1000 μm^2/s V [16]. In contrast, the effective mobility we consider here quantifies the actual transport of particles from one electrode to the other in the presence of screening effects and under the influence of both EP and EO.

We compare important parameters such as switching time, particle velocity, and effective mobility of particles in our approach with those of existing electronic display technologies, as shown in Table 1. In the first row of the table, we provide values for the typical e-ink technology, used in a wide range of commercially available electronic paper displays, which is based on fluidic capsules placed between parallel electrodes. In one of the first publications on this technology, a typical separation between the electrodes of d ~40 μm is described, along with a switching time scale of 100 ms and a particle velocity of 400 μm/s at an applied voltage of 94.4 V [17]. This corresponds to an effective mobility of $\mu_{\text{eff.}} \sim 169$ μm^2/Vs. The second row of the table refers to a publication on a full color electrophoretic display with improved update time, in which switching times of 250-500 ms were achieved using a driving voltage of 17-30 V [18]. With the typical electrode separation of d ~20–30 μm, we obtain an effective mobility of $\mu_{\text{eff.}} \sim 26$–$211$ μm^{2}Vs.

As shown in the last row of the table, in the current work we observe an effective transport velocity of the particles of $u \sim 100$ μm/s, which corresponds to an effective mobility of $\mu_{\text{eff.}} \sim 1000$ μm^2/Vs.

The results thus indicate that our system outperforms existing technologies in terms of effective mobility, which we believe can be further improved upon through the use of geometries optimized to reduce the switching time and thus improve display update time.

Finally, we also find a good agreement between experimental and numerical results of electrokinetically driven particle motion in fluidic cells due to the combined actions of EO and EP. This validation of the simulation results implies that the simulation model can be put to work, by changing and testing different parameters such as electrode design or channel height, to identify optimized designs that lead to enhanced particle motion in electrokinetic devices. Using this approach could thus enable reducing the switching time for displaying information, and thus extend the use of electrokinetic displays towards video applications in the future. Our work is also interesting from a fundamental scientific point of view, with possible implications for other experimental systems, as it sheds light on how in general the interplay between different electrokinetic phenomena governs the motion of colloidal particles in nonpolar solvents.

CRediT authorship contribution statement

Mohammad Khorsand Ahmadi: Conceptualization, Data curation, Formal analysis, Investigation, Methodology, Validation, Visualization, Writing – original draft, Writing – review & editing, Software. **Wei Liu:** Formal analysis, Investigation, Software, Validation, Visualization, Writing – review & editing. **Jan Groenewold:** Conceptualization, Methodology, Project administration, Supervision, Writing – review & editing, Data curation, Formal analysis, Software, Validation. **Jaap M.J. den Toonder:** Conceptualization, Funding acquisition, Project administration, Supervision, Writing – review & editing. **Alex Henzen:** Funding acquisition, Project administration, Supervision, Conceptualization, Data curation, Formal analysis, Methodology, Validation, Writing – review & editing. **Hans M. Wyss:** Conceptualization, Data curation, Formal analysis, Investigation, Methodology, Project administration, Software, Supervision, Validation, Writing – original draft, Writing – review & editing.

Declaration of competing interest

The authors declare that they have no known competing financial interests or personal relationships that could have appeared to influence the work reported in this paper.

Data availability

Data will be made available on request.

Acknowledgements

This work was supported by the Nederlandse Organisatie voor Wetenschappelijk Onderzoek under the NWO-GDST Grant, “Electro-optical full colour display based on nano-particle dispersions”, Grant

No. 729.001.042. Wei Liu gratefully acknowledges financial support from the China Scholarship Council (202106750027).

Appendix A. Supplementary material

Supplementary material related to this article can be found online at https://doi.org/10.1016/j.jcis.2024.02.194.

References

[1] S. Haeberle, R. Zengerle, Microfluidic platforms for lab-on-a-chip applications, Lab Chip 7 (9) (2007) 1094–1110.
[2] Q. Ren, Y. Wang, X. Lin, C.L. Chan, Ac electrokinetic induced non-Newtonian electrothermal blood flow in 3d microfluidic biosensor with ring electrodes for point-of-care diagnostics, J. Appl. Phys. 126 (8) (2019) 084501.
[3] M. Prasad, F. Strubbe, F. Beunis, K. Neyts, Electrokinetics and behavior near the interface of colloidal particles in non-polar dispersions, Soft Matter 13 (33) (2017) 5604–5612.
[4] G.N. Smith, J. Eastoe, Controlling colloid charge in nonpolar liquids with surfactants, Phys. Chem. Chem. Phys. 15 (2) (2013) 424–439.
[5] X. Wang, C. Cheng, S. Wang, S. Liu, Electroosmotic pumps and their applications in microfluidic systems, Microfluid. Nanofluid. 6 (2) (2009) 145–162.
[6] P. Modarres, M. Tabrizian, Phase-controlled field-effect micromixing using ac electroosmosis, Microsyst. Nanoeng. 6 (1) (2020) 1–11.
[7] Z. Wu, D. Li, Micromixing using induced-charge electrokinetic flow, Electrochim. Acta 53 (19) (2008) 5827–5835.
[8] M.F. Hsu, E.R. Dufresne, D.A. Weitz, Charge stabilization in nonpolar solvents, Langmuir 21 (11) (2005) 4881–4887.
[9] F. Beunis, F. Strubbe, M. Karvar, O. Drobchak, T. Brans, K. Neyts, A.R. Verschueren, Electric charging of inverse micelles in a nonpolar liquid with surfactant, Colloids Surf. A, Physicochem. Eng. Asp. 440 (2014) 10–19.
[10] J. Lyklema, Fundamentals of Interface and Colloid Science: Soft Colloids, vol. 5, Elsevier, 2005.
[11] S. Chen, N. Angarita-Jaimes, D. Angarita-Jaimes, B. Pelc, A. Greenaway, C. Towers, D. Lin, D. Towers, Wavefront sensing for three-component three-dimensional flow velocimetry in microfluidics, Exp. Fluids 47 (4) (2009) 849–863.
[12] Z. Liu, M.F. Speetjens, A.J. Frijns, A.A. van Steenhoven, Application of astigmatism μ-ptv to analyze the vortex structure of ac electroosmotic flows, Microfluid. Nanofluid. 16 (3) (2014) 553–569.
[13] J.C. Crocker, B.D. Hoffman, Multiple-particle tracking and two-point microrheology in cells, Methods Cell Biol. 83 (2007) 141–178.
[14] J.C. Crocker, D.G. Grier, Methods of digital video microscopy for colloidal studies, J. Colloid Interface Sci. 179 (1) (1996) 298–310.
[15] M. Raffel, C.E. Willert, S. Fulvio, C.J. Kahler, S.T. Wereley, J. Kompenhans, Particle Image Velocimetry: A Practical Guide, Springer, 2007.
[16] S. Kholghi Eshkalak, M. Khatibzadeh, E. Kowsari, A. Chinnappan, W.A.D.M. Jayathilaka, S. Ramakrishna, Overview of electronic ink and methods of production for use in electronic displays, Opt. Laser Technol. 117 (2019) 38–51.
[17] B. Comiskey, J.D. Albert, H. Yoshizawa, J. Jacobson, An electrophoretic ink for all-printed reflective electronic displays, Nature 394 (6690) (1998) 253–255.
[18] S.J. Telfer, W.T. Chen, M.D. McCreary, 67-1: full-color electrophoretic displays with improved update time, SID Symp. Dig. Tech. Pap. 52 (1) (2021) 995–998.